Hindawi
Shock and Vibration
Volume 2022, Article ID 6221067, 18 pages
https://doi.org/10.1155/2022/6221067

*Research Article*

# Research on the Control Method of Force Servo System of Liquid Hydrostatic Guide Oil Film Thickness Test Bench for Machine Tools

**Xu Fang, Youmin Wang, and Bo Zhu**

*College of Mechanical Engineering, Anhui Polytechnic University, Wuhu, Anhui, China*

Correspondence should be addressed to Youmin Wang; wymtlf@ahpu.edu.cn

Received 28 April 2022; Revised 25 July 2022; Accepted 22 August 2022; Published 6 October 2022

Academic Editor: Rozaimi Ghazali



The test bench was designed to solve the problem of measuring the oil film thickness of the liquid hydrostatic guideway of machine tools. And based on the fast overshoot of the classical PID control, introducing the self-antidisturbance control algorithm, this study established a mathematical model of the test bench electro-hydraulic servo control system. At the same time, this paper also designed a specific structure of the self-turbulence controller, which adopts optimal quadratic control, pole configuration, PID control, and self-turbulence control to study the control methods of the test bench electro-hydraulic servo system, respectively, and uses the SIMULINK module to establish the system simulation model of the above-mentioned four control methods of the test bench. Simulation results of the test bench control system show that the response speed of the self-turbulence control is 0.4 seconds, 0.2 seconds, and 4.4 seconds faster than PID control, pole configuration, and optimal quadratic control, respectively, and the overshoot is significantly reduced. Finally, the test bench was built to complete the experiments, and the experimental results showed that the followability of the loading force and thickness detection accuracy of the test bench were better after adding the self-turbulence control algorithm and the stability of the oil film thickness was significantly improved by the test bench electro-hydraulic servo control system.

## 1. Introduction

In practice, the hydrostatic guide will be subject to various variable loads so that the oil film thickness is unstable, and the oil film thickness instability will have a negative effect on the oil film stiffness and bearing capacity [1]. Maintaining the oil film thickness in ideal conditions is an important factor in improving the accuracy of the guide rail [2]. The traditional machine tool liquid hydrostatic guide oil film thickness detection test bench mainly uses fixed-point detection to detect the oil film thickness. It cannot simulate the real-time changes of cutting force in machine tool processing, so the detection obtained is neither real-time nor has automatic detection capability. In addition, the hydraulic control system of the test bench is mainly quadratic optimal control, pole configuration, PID control, etc., which can no longer meet the requirements of the existing test bench to detect the oil film thickness. Therefore, it is necessary to propose a new test bench hydraulic control system for detecting oil film thickness test bench.

Wu [3] and others have studied the state stochastic linear quadratic optimal control and proposed that the optimal control strategy is the segmental affine function of the system state. Dario [4] proposed a new method of inverse resonance assignment and regional pole configuration for linear time-invariant vibration systems. Although many scholars have used quadratic optimal control and pole configuration to solve relevant practical engineering problems, they have not yet introduced this control method into the design of hydraulic guideways. Yang [5] and Ji-min [6] mainly used classical PID control of the hydraulic system to meet the usage requirements. However, this control has a relatively poor anti-interference capability. Since the electro-hydraulic servo

system model has indeterminacy for some more important equipment, the traditional control algorithm no longer meets the requirements of the system use [7]. Guo [8] used anti-interference control to achieve accurate control of the servo system. This control has been studied academically in several aspects, but only at the theoretical level, and has not yet been applied in practice. Goforth et al. [9] and Wang et al. [10]. used a self-anti-disturbance control algorithm to optimize the system performance, which comes with a specific structure and error feedback mechanism for the control technique. After that, Jingqing Han found that the integrator series type structure of the control system was available for both linear and nonlinear systems in the corresponding feedback case and pointed out that the feedback can be taken to identify the system, and they regarded the system function as state feedback and proposed the establishment method of the expansion state observer [11]. In summary, on the basis of the testbed control model establishment, many intelligent algorithms have emerged, and the key to their performance is whether they can suppress disturbances well.

In this paper, in order to study the optimal control method of the test bench for liquid hydrostatic guideway oil film thickness inspection of machine tools, the general scheme design of the test bench was designed and the three-dimensional model of the test bench was established by NX. Based on the hydraulic control valve flow equation, the cylinder flow continuity equation, and the force balance equation between the cylinder and the load, this study obtained the mathematical model of the test bench control system and simulated the system. This paper used quadratic optimal control, pole configuration, PID control, and self-anti-disturbance control to optimize the electro-hydraulic servo system of the test bench, respectively. The SIMULINK module was also used to simulate the test bench control system, and the response curves of the four control strategies were obtained. The results showed that the response speed of the self-turbulence control is 0.4 sec, 0.2 sec, and 4.4 sec faster than that of the PID control, pole configuration, and quadratic optimal control, respectively, and the overshoot is significantly reduced. Finally, this paper built a test bench to complete the experiment, and the experimental results show that the anti-interference ability of the test bench electro-hydraulic force servo control system has been improved after adding the self-antidisturbance control algorithm, at which time the test bench loading force following and thickness detection accuracy is the highest, which also leads to a significant improvement in the oil film thickness stability.

## 2. Overall Design of the Test Bench

This paper designs a test bench for detecting oil film thickness to study the optimal control method for the test bench for detecting oil film thickness of liquid hydrostatic guideways of machine tools. The overall scheme of this test bench mainly includes the design of the mechanical structure and the design of the hydraulic control system.

*2.1. Mechanical Structure Design.* The mechanical structure of the oil film thickness inspection test bench is mainly divided into (1) a horizontal moving module and (2) a vertical moving module, which is used to simulate the variation of the cutting force of the machine tool [3], and the three-dimensional model of the test bench mechanical structure is shown in Figure 1. Lab table rails have certain errors in their directions of width and length when they are designed. In addition, when the hydraulic guide consists of opposite pads, the oil film stiffness plays a crucial role in the error averaging effect [12].

The horizontal movement module consists of an electric motor, a first coupling, a first ball screw, a dynamic guide, a static guide fixed to the base, and left and right bearing supports assembled on both ends of the static guide. When the first motor is energized, the dynamic guide can make horizontal reciprocating movements along with the static guide.

The vertical movement module consists of a handle, a handle bracket, a second ball screw, a first slider, a second slider, a linkage, a column, and a hydraulic cylinder. The second slider is assembled on the column and can move reciprocally along the column groove, and it is connected to the first slider by a connecting rod.

*2.2. Design of the Hydraulic Control System of the Test Bench.* The hydraulic control system design of the test stand contains (a) an electro-hydraulic servo control system (b) and an oil film thickness detection system. The schematic diagram of the hydraulic control system is shown in Figure 2.

The size of the cutting force of the machine is simulated by the electro-hydraulic force servo control system of the test bench. When the electro-hydraulic servo control circuit works, this study takes the spool opening and direction to adjust the piston rod load and the cutting force of the guide [13]. The oil film thickness detection system is connected to the computer through the pressure sensor, and the measurement data are processed by the computer. According to the schematic diagram of the hydraulic control system of the test bench, after calculating the selection of each component in the hydraulic system, the hydraulic control system components of the test bench model are as listed in Table 1. Simulation of hydraulic control systems using AMESim (Advanced Modeling Environment for performing Simulations of engineering systems) is used to continuously optimize the dynamic performance of the system by adjusting the parameters of each component, thus improving the efficiency of the equipment [14, 15]. The system is set at a rated pressure of 6 MPa, a nominal pressure of 10 KN, and a piston rod stroke of 100 mm left and right.

## 3. Modeling and Simulation of the Electro-Hydraulic Servo Control System of the Test Bench

In this paper, to get the mathematical model of the control system of the test bench, the hydraulic control valve flow equation, the cylinder flow continuity equation, and the

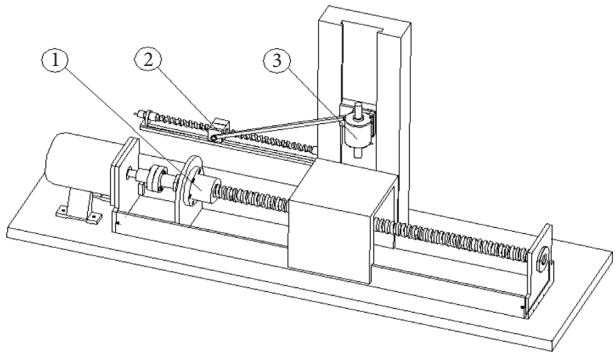


Figure 1: 3D model of the mechanical structure of the test bench.

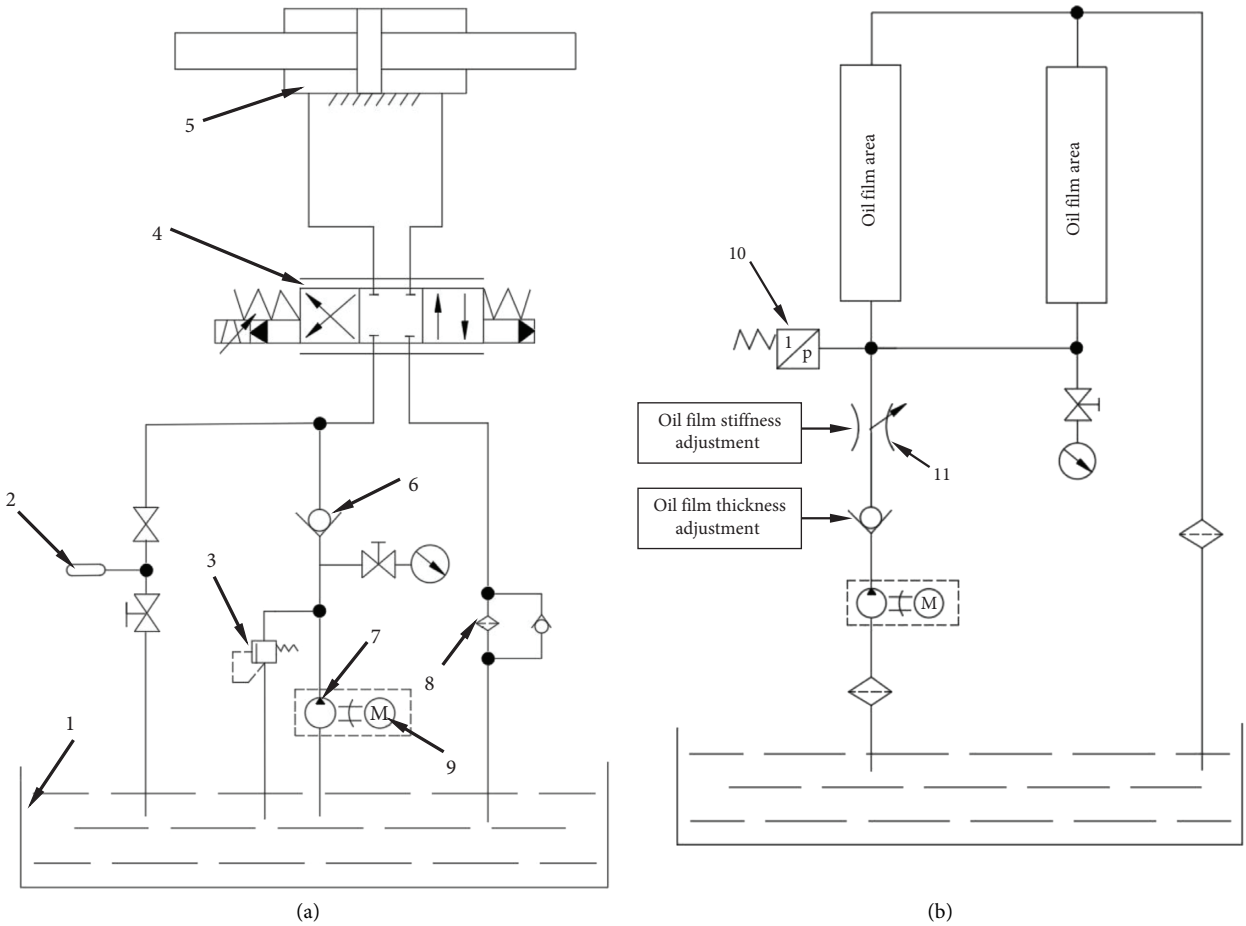


Figure 2: Principle diagram of hydraulic control system of test bench. 1: tank; 2: accumulator; 3: relief valve; 4: electro-hydraulic servo valve; 5: hydraulic cylinder; 6: check valve; 7: quantitative pump; 8: filter; 9: motor; 10: pressure sensing; 11: throttle valve.

force balance equation between the cylinder and the load are established, respectively, combined with the control system deviation voltage signal equation and the feedback link pressure sensor equation to get the transfer function of the system, and finally the simulation analysis of the system.

*3.1. Modeling of the Electro-Hydraulic Servo Control System of the Test Bench.* The electro-hydraulic force servo control is used to simulate the cutting force during the actual operation of the machine tool and add variable load to the dynamic guide. The schematic diagram of the electro-hydraulic servo control system of the test bench is shown in

Table 1: Hydraulic control system component models of the test bench.

| Hydraulic component name | Hydraulic component parameters | Hydraulic component models |
|---|---|---|
| Hydraulic cylinder | $D = 63$ mm $d = 35$ mm | — |
| Hydraulic pumps | — | CBGF1018 gear pumps |
| Electric motors | Power rating 5.5kw | Y2-132S-4 |
| Electro-hydraulic servo valve | Rated flow rate 20 | 4WSE2EM6-2X |
| One-way valve | Rated flow rate 30 | RVP10-30B |
| Servo amplifier | — | NB2000 |
| Relief valve | Rated flow rate 30 L/min | DBDS6G10/200 |
| Pressure sensors | Measurement range 0~1000 kg, voltage 0~10 V | Seamless steel pipe: inner diameter 16 mm, wall thickness 2 mm |

Figure 3. The block diagram of the machine's hydrostatic guide control system is shown in Figure 4.

This paper establishes the hydraulic control valve flow equation, the cylinder flow continuity equation, and the force balance equation between the cylinder and the load, respectively.

$$q_L = K_q x_v - K_c p_L, \tag{1}$$

$$q_L = A_p \frac{dx_p}{dt} + C_{tp} p_L + \frac{V_t}{4\beta_e} \frac{dp_L}{dt}, \tag{2}$$

$$A_p p_L = m_t \frac{d^2 x_p}{dt^2} + B_p \frac{dx_p}{dt} + K x_p. \tag{3}$$

In the formula, $q_L$ is the load flow ($m^3/s$); $K_p$ is the flow gain coefficient ($m^3/s$); $x_v$ is the valve spool displacement (m); $K_c$ is the low-pressure gain coefficient ($m^5/N\bullet s$); $P_L$ is the load pressure (Pa); $A_p$ is the effective working area of hydraulic cylinder ($m^2$); $x_p$ is the hydraulic rod displacement (m); $C_{tp}$ is the total leakage coefficient of hydraulic cylinder ($m^5/N\bullet s$); Vt is the total compressed volume ($m^3$); $\beta_e$ is the effective bulk modulus of elasticity (Pa); $m_t$ is the load quality (kg); $B_p$ is the load damping factor ($N\bullet s/m$); and $K$ is the load spring stiffness (N/m).

The Laplace transform of equations (1)–(3) yields

$$\begin{cases} Q_L = K_q X_v - K_c P_L, \\ Q_L = A_p s X_p + C_{tp} P_L + \dfrac{V_t}{4\beta_e} s P_L, \\ A_p P_L = m_t s^2 X_p + B_p s X_p + K X_p. \end{cases} \tag{4}$$

This paper establishes the control system deviation voltage signal equation and feedback link pressure sensor equation, respectively.

$$U_e = U_r - U_f, \tag{5}$$

$$U_f = K_{fF} F_g. \tag{6}$$

In the formula, $U_r$ is the input voltage signal (V); $U_f$ is the feedback voltage signal (V); $k_{fF}$ is the pressure sensor gain (V/N); and $F_g$ is the output force of the cylinder (N).

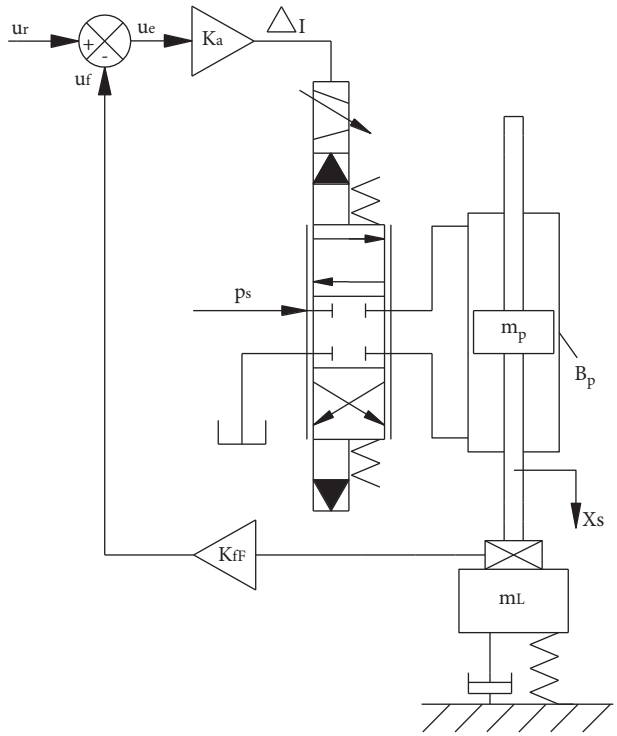


Figure 3: Electro-hydraulic servo control system schematic.

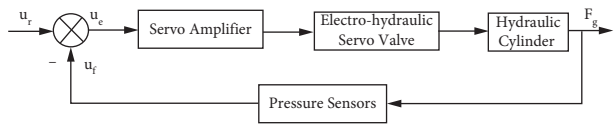


Figure 4: Block diagram of the machine's hydrostatic guide control system.

The output current of the amplifier, considering only the quiescent performance, is

$$\Delta I = K_a U_e. \tag{7}$$

In the formula, $K_a$ is the servo amplifier gain (A/V).

According to the above-given equation, the electro-hydraulic servo valve transfer function is

$$\frac{X_v}{\Delta I} = K_{sv} G_{sv}(s). \tag{8}$$

In the formula, $X_v$ is valve spool displacement (m); $K_{sv}$ is hydraulic valve gain ($m^3/s•A$); and $G_{sv}$ (s) is $K_{sv} = 1$.

The block diagram of the system is shown in Figure 5 based on equations (4)–(8). Here, $K_{ce} = K_c + C_{tp}$.

Servo valves consider dynamic performance. The system model is complex with fifth-order, fourth-order, and third-order functions, because the electro-hydraulic servo valve fast response generally only considers the static performance directly as a proportional link. According to the stage of valve spool displacement to cylinder output force in Figure 5 to simplify the control system block diagram, the system mathematical model is simplified as

$$G(s) = \frac{K_a K_{sv}\left(K_q/K_{ce}\right) A_p K_f F\left(s^2/w_m^2\right) + 1}{\left((s/w_r) + 1\right)\left(\left(s^2/w_0^2\right) + \left(2\xi_0/w_0\right)s + 1\right)}. \quad (9)$$

The parameter assignment and simplification of equation (9) give the transfer function

$$G(s) = \frac{4.07 \times 10^{-3} s^2 + 3.25}{5.87 \times 10^{-5} s^3 + 5.75 \times 10^{-3} s^2 + 3.50s + 1}. \quad (10)$$

*3.2. Simulation of the Electro-Hydraulic Servo Control System of the Test Bench.* Simulation of the system transfer function using SIMULINK yields the system step response curve shown in Figure 6.

As can be seen from Figure 6, the control performance of the system is very unsatisfactory. When the input unit step signal is applied, the system can be stabilized in about 20.5 s, which is a long time, and its input and output signals do not match, which needs to be optimized.

## 4. Test Bench Electro-Hydraulic Servo Control System Optimization Method Comparison Analysis

The article is based on the comprehensive optimization of classical PID control based on the self-turbulence control algorithm. This study designs the specific structure of the self-turbulence controller and uses quadratic optimal control, pole configuration, PID control, and self-turbulence control to optimize the electro-hydraulic servo system of the test bench, respectively. Finally, the SIMULINK module is used to simulate the test bench control system and obtain the response curves under the four control strategies.

*4.1. Linear Quadratic Optimal Control.* The principle of optimal control is to find a control variable $u(t)$ that has a small value and can satisfy the minimum system error $x(t)$, so that the system output quantity follows the input quantity quickly and with low energy consumption [16]. According to Pontryagin's principle, to be able to obtain the index minimal value, the essence of quadratic optimal control is to approximate the feedback $K(t)$ added to the original system. In this paper, the feedback of the optimal regulator is used to approximate the optimization, then the simplified optimal control rate is

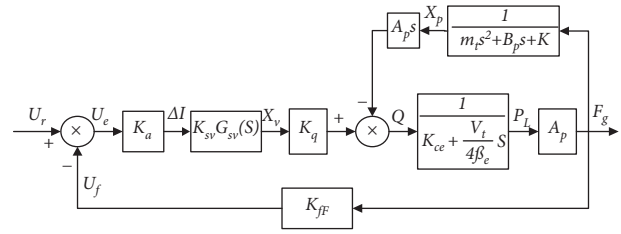


Figure 5: Block diagram of the control system.

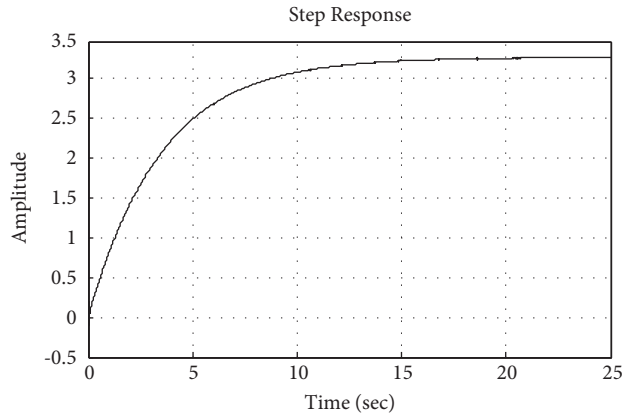


Figure 6: System step response curve.

$$u(t) = -K(t)x(t) = R^{-1}(t)B^T(t)P(t)x(t). \quad (11)$$

The algebraic equation of the Riccati matrix is

$$PA + A^T P - PBR^{-1}B^T P + Q = 0. \quad (12)$$

In the formula, $A$ is the system matrix; $B$ is the control matrix; $Q$-$R$ is the weighted matrix; and $P$ is the equation solution.

The optimal weight matrix selected in this paper is $Q = \text{diag}\{275000,1,1\}$ and $R = 0.0001$.

The optimized system matrix is

$$A - BK = \begin{bmatrix} 0 & 1 & 0 \\ 0 & 0 & 1 \\ -55138 & -59727 & -141 \end{bmatrix}. \quad (13)$$

Using MATLAB to simulate the transfer function under quadratic optimal control, the step response curve of the system after linear quadratic optimal control is as shown in Figure 7.

As can be seen from Figure 7, the system reaches stability at 5.6 s. After the optimization of the oil film thickness control system by quadratic optimal control, the system stabilization time is shortened by 14.9 s. The control performance is greatly improved, but the system reaches its stabilization time is longer.

*4.2. Pole Optimization Configuration.* After adding the state feedback gain matrix $K = [k1\ \ k2\ \ k3]$, the characteristic polynomial is

$$\alpha(\lambda) = \det(\lambda I - A + bK) = \left\| \begin{bmatrix} \lambda & 0 & 0 \\ 0 & \lambda & 0 \\ 0 & 0 & \lambda \end{bmatrix} - \begin{bmatrix} 0 & 1 & 0 \\ 0 & 0 & 1 \\ -17036 & -59625 & -98 \end{bmatrix} + \begin{bmatrix} 0 & 0 & 0 \\ 0 & 0 & 0 \\ k_1 & k_2 & k_3 \end{bmatrix} \right\| \tag{14}$$
$$= \lambda^3 + (k_3 + 98)\lambda^2 + (k_2 + 59625)\lambda + (k_1 + 17036).$$

The key to controlling system performance is determined by the dominant pole, while the role of the far pole is negligible [17]. Therefore, the testbed control system can be equivalently replaced by a second-order control system containing the dominant pole pair.

From the dynamic indicators $\sigma_p\%$ and $t_s$ to determine the location of the expected dominant pole,

$$\sigma_p\% = e^{-\pi\xi/\sqrt{1-\xi^2}} \times 100\%. \tag{15}$$

In the formula, $\sigma_p\%$ is the maximum overshoot and $\xi$ is the damping $(0 < \xi < 1)$.

Let the allowable error of the control system be 5%; then,

$$t_s = \frac{3}{\xi\omega_n}. \tag{16}$$

In the formula, $t_s$ is the adjustment time (s) and $\omega_n$ is the undamped frequency (rad/s).

The expected dominant pole of the system is

$$\lambda_{1,2} = -\xi\omega_n \pm j\omega_n\sqrt{1-\xi^2}. \tag{17}$$

In the formula, $\lambda_{1,2}$ are the expectations that dominate the poles.

Because of the maximum overshoot of the system $\sigma_p\% \leq 5\%$, adjustment time $t_s \leq 0.5$ s; therefore, the expected dominant pole of the control system is obtained from the following equation with $\lambda 1$ and $\lambda 2$.

$$\begin{cases} \sigma_p\% = e^{-\pi\xi/\sqrt{1-\xi^2}} \times 100\% \leq 5\%, \\ t_s = \dfrac{3}{\xi\omega_n} \leq 0.5. \end{cases} \tag{18}$$

The solution is

$$\begin{cases} \xi \geq 0.69, \\ \xi\omega_n \geq 6. \end{cases} \tag{19}$$

Taking $\xi = 0.707$ and $\xi\omega_n = 6$, then

$$\lambda_{1,2} = -\xi\omega_n \pm j\omega_n\sqrt{1-\xi^2} = -6 \pm j6. \tag{20}$$

Make the third pole $\lambda 3 = 10\mathrm{Re}[\lambda_1] = -60$. Therefore, there is $\alpha^*(s) = (s+60)(s+6-j6)(s+6+j6) = s^3 + 72s^2 + 792s + 4320$. By $\alpha(s) = \alpha^*(s)$, we obtain

$$K = [\, k_1 \;\; k_2 \;\; k_3 \,] = [\, -26 \;\; -58833 \;\; -12716 \,]. \tag{21}$$

The step response curve of the system after the pole configuration is obtained using SIMULINK module simulation as shown in Figure 8.

According to Figure 8, it can be seen that the system reached stability at 1.4 seconds. After the oil film thickness control system was optimized by the pole configuration, the stabilization time was shortened by 19.1 seconds, and the control performance was significantly improved, but the control system showed an overshoot phenomenon.

*4.3. PID Control.* The classical PID control has been widely used because of its simple structure and easy parameter positive determination [18, 19]. PID control starts by determining the proportionality factor $K_p$. Let the integral and differential constants be 0. Gradually increase the proportional gain from zero until the response curve oscillates and then slowly decrease the data until the oscillation stops. Take 30%–70% of the proportional gain as the system proportionality factor. Here, 60% is taken. After the proportionality factor is decided, the larger value is chosen as the initial value of the integration constant $K_i$ of the system. By repeatedly adjusting the system to stop the oscillation, 150%–180% of the integration constant is taken as the final value of the integration constant of the system, which is 165% at this time. In the case of the system output force, the differential constant $K_d$ is usually selected as 0. Finally, the parameters of the PID controller are selected as $K_p = 11.17$, $K_i = 63.11$, and $K_d = 0$.

The PID control step response curve of the system using SIMULINK simulation is shown in Figure 9.

As can be seen from Figure 9, the system performance is improved somewhat by using PID control. The system can reach stability at 1.6 s when a unit step signal is an input, and its input and output signals match, but the system is accompanied by a certain amount of overshoot.

*4.4. Self-Antidisturbance Control.* In order to further improve the control effect of the test bench control system, a self-antidisturbance control algorithm is introduced based on the fast overshoot of the PID control [20], and the specific structure of the self-antidisturbance controller is analyzed and designed. The block diagram of the self-antidisturbance control designed in this paper is shown in Figure 10.

*4.4.1. Analysis of Self-Tampering Controllers.* The self-resistant controller consists of three modules, the tracking differentiator (TD), the expanded state observer (ESO), and the control rate (CL). What can be learned from the system state space expression is that the controlled object is in the third order, so the tracking differentiator is third order and the dilated state observer is fourth-order.

To improve the dynamic characteristics of this energy control system, the required poles are configured using state

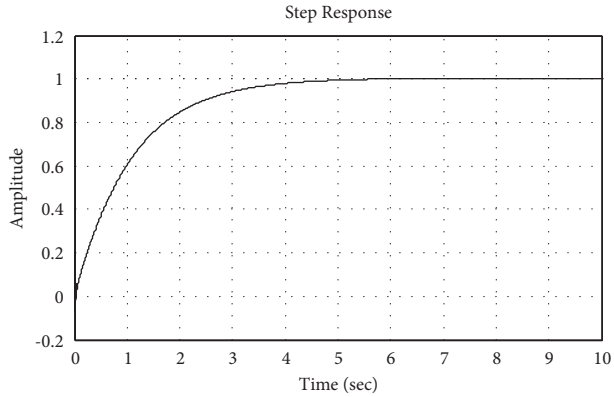


Figure 7: Step response curve of the system after quadratic optimal control.

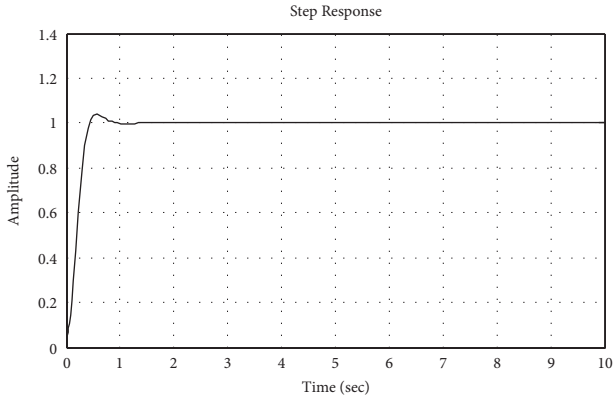


Figure 8: Step response curve of the system after pole configuration.

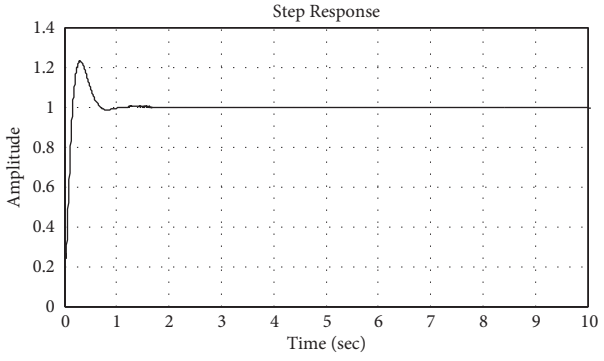


Figure 9: System PID control step response curve.

feedback. If the zero-point configuration of the control system can be achieved, the dynamic performance of the control system can be better improved. However, the zero-point configuration requires the use of differential signals, and the general differential cannot filter the noise well and cannot be used for zero-point configuration, while the tracking differential can filter the noise well and its differential signal can be used for zero-point configuration [21].

The tracking differentiator follows the given signal and obtains its differential equation. Arranging the transition process through the tracking differentiator prevents overshoot due to sudden changes in the given signal and makes the controlled object approach the target smoothly, thus improving the stability of the control system. By eliminating the poles of the system with the configured zeros, the system can be viewed as a control system approximating 1. Let the string-level object be

$$y = \frac{1}{p_1(s)} \frac{1}{p_2(s)} u. \tag{22}$$

Assume that $P_2(s)$ is known and let the virtual control volume be

$$U(t) = \frac{1}{p_2(s)} u. \tag{23}$$

Then, the control system becomes

$$y = \frac{1}{p_1(s)} U(t). \tag{24}$$

If the virtual control quantity $U(t)$ is determined, the actual control quantity is

$$u = p_2(s) U(t). \tag{25}$$

In the formula, $P_1(s)$ and $P_2(s)$ are polynomials.

The virtual control volume $U(t)$ is determined by applying a self-turbulent controller design approach to the control subsystem $y = U(t)/P_1(s)$, which thus allows for a certain range of uncertainties to exist.

Let the mathematical model of the controlled object contain zeros and poles. Its general form is

$$y = \frac{q(s)}{p(s)} u. \tag{26}$$

Let the virtual control volume $U(t) = q(s)$u; then, the system becomes $y = U(t)/P(s)$; hence, the actual control volume becomes $u = U(\mathrm{t})/q(s)$.

If the controlled object conforms to the minimum phase system, then $q(s)$ belongs to a stable polynomial and is known. At this point, a self-antidisturbance controller can be used to determine the virtual control quantity $U(t)$, and then the problem can be solved by considering $U(t)$ as the input and solving the system $u = U(t)/q(s)$ to obtain the actual control quantity $u(t)$.

Based on the above-mentioned analysis, the zero-pole diagram of the controlled object is derived using MATLAB as shown in Figure 11.

From Figure 11, it can be seen that the system model has no zeros and poles in the positive part of the complex plane, so it belongs to the minimum phase system. In this case, it is possible to determine the virtual control quantity $U(t)$ by a self-antidisturbance controller, and then the $U(t)$ is considered as an input to solve the system $u = U(t)/q(s)$ to obtain the actual control quantity.

From the control system transfer function is known to satisfy the cubic polynomial $p_3(s) = s_3 + a_3 s_2 + a_2 \mathrm{s} + a_1$, and at

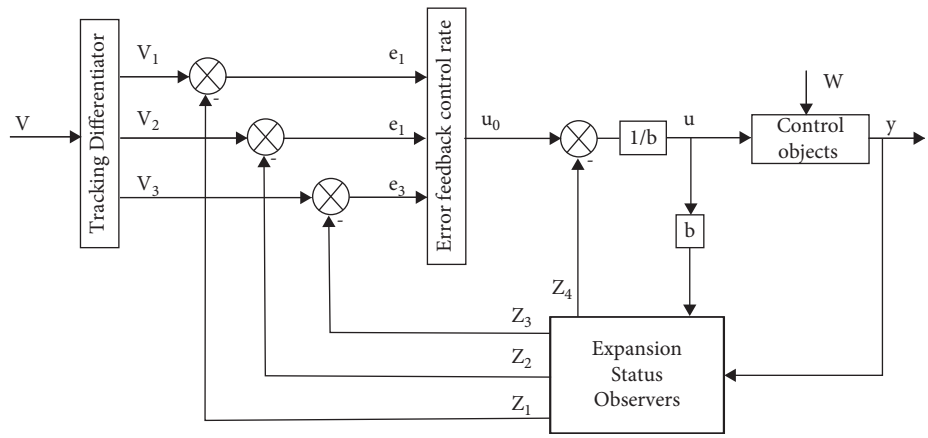


Figure 10: Control block diagram of the third-order self-tampering controller.

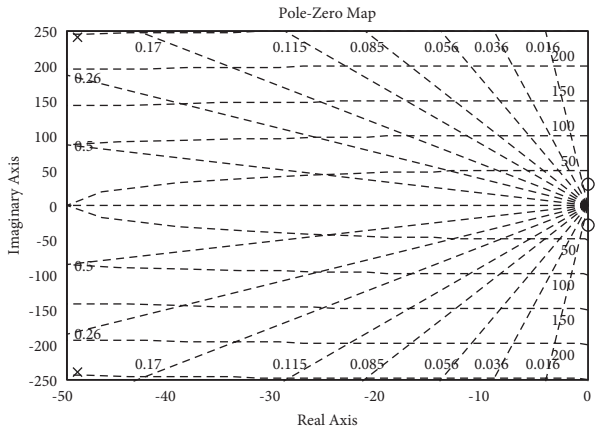


Figure 11: Zero-pole diagram of the controlled object.

this time, the parameters $a_1$, $a_2$, and $a_3$ are known; the algorithm of the third-order tracking differentiator can be obtained as

$$\begin{cases} fs = -r\left(r\left(r\left(v_1 - v(t)\right) + 3v_2\right) + 3v_3\right), \\ v_1 = v_1 + hv_2, \\ v_2 = v_2 + hv_3, \\ v_3 = v_3 + hfs, \\ U(t) = v_1(t). \end{cases} \tag{27}$$

In the formula, $r$ is the fast factor and $h$ is the sampling step size.

The expansive state observer follows the control system output, observes in real time the state conditions of each order of the object of study and the total system disturbance, and compensates for the disturbance accordingly [22]. If the system is subject to unknown disturbances, the control object is uncertain [23, 24]. The uncertain objects are

$$\begin{cases} x^{(n)} = f\left(x, \dot{x}, \cdots, x^{(n-1)}, t\right) + w(t) + bu, \\ y = x(t). \end{cases} \tag{28}$$

In the formula, $f(x, x', \ldots, x^{(n-1)}, t)$ is the system unknown function; $\omega(t)$ is the unknown perturbation; $u$, $y$ are system inputs and outputs; and $b$ is the control gain.

The dilation state observer in this paper is fourth-order, and under linear conditions, the control system fourth-order dilation state observer algorithm is

$$\begin{cases} e = z_1 - y, \\ z_1 = z_1 + h\left(z_2 - \beta_{01}e\right), \\ z_2 = z_2 + h\left(z_3 - \beta_{02}e\right), \\ z_3 = z_3 + h\left(z_4 - \beta_{03}e + bu\right), \\ z_4 = z_4 + h\left(-\beta_{04}e\right). \end{cases} \tag{29}$$

In the formula, $\beta_{01}$, $\beta_{02}$, $\beta_{03}$, and $\beta_{04}$ are expansion state observer parameters and $e$ is error term. In the control system, the ESO contains four output variables, $z_1$ following the system output $y$, $z_2$ following $y'$, $z_3$ following $y''$, and $z_4$ following the system integrated disturbance, using feedforward methods to compensate for the disturbance [23].

The transfer relation from input to the output of the expansion state observer is

$$\begin{cases} z_1 = w_1(s)y = \dfrac{\beta_{01}s^3 + \beta_{02}s^2 + \beta_{03}s + \beta_{04}}{s^4 + \beta_{01}s^3 + \beta_{02}s^2 + \beta_{03}s + \beta_{04}}y, \\ z_2 = w_2(s)y = \dfrac{\beta_{02}s^3 + \beta_{03}s^2 + \beta_{04}s}{s^4 + \beta_{01}s^3 + \beta_{02}s^2 + \beta_{03}s + \beta_{04}}y, \\ z_3 = w_3(s)y = \dfrac{\beta_{03}s^3 + \beta_{04}s^2}{s^4 + \beta_{01}s^3 + \beta_{02}s^2 + \beta_{03}s + \beta_{04}}y, \\ z_4 = w_4(s)y = \dfrac{\beta_{04}s^3}{s^4 + \beta_{01}s^3 + \beta_{02}s^2 + \beta_{03}s + \beta_{04}}y. \end{cases} \tag{30}$$

In order to achieve a certain estimation accuracy, it is necessary to choose larger gain coefficients, gain coefficients $\beta_{01}$, $\beta_{02}$, $\beta_{03}$, and $\beta_{04}$ which need larger values so as to satisfy the high gain observer mode.

The error feedback control rate compares the state variables obtained from the transition process, each order of differentiation, and the dilated state observer for a given signal of the system, and then the deviation signal is algorithmically derived from the control quantity. The algorithm is

$$\begin{cases} e_1 = v_1 - z_1, \\ e_2 = v_2 - z_2, \\ e_3 = v_3 - z_3, \\ u_0 = \beta_{11} e_1 + \beta_{12} e_2 + \beta_{13} e_3. \end{cases} \tag{31}$$

In the formula, $\beta_{11}$ is the control rate parameter and $e_i = v_i - z_i$ is the state error.

So the algorithm for the control volume is

$$u = \frac{(u_0 - z_4)}{b}. \tag{32}$$

*4.4.2. Creation of the Self-Tampering Controller Subsystem.* When the controller used for system optimization is complex, a subsystem is used to split the complex self-resistant controller module into a tracking differentiator submodule, an expansion state observer submodule, and an error feedback control rate submodule, thus making the complex self-resistant controller seen more clearly and simply.

The tracking differentiator subsystem is created, where the tracking differentiator subsystem module is specifically set with the following settings: function name TD3_L; function parameters are *r*, *h*; function module is TD3_L; and the TD3_L. m program is added inside Edit.

In the TD3_L subsystem packaging process, Transparency in the Icon & Ports property is set to Transparent, and the Drawing commands section is disp ("TD3_L"); Prompt in the Parameters property; the modular composition of the tracking differentiator subsystem is shown in Figure 12, and the TD3_L subsystem module after the package is completed is shown in Figure 13.

We created the dilated state observer subsystem, where the tracking differentiator subsystem module is specifically set with the following settings: function name ESO4_L; function parameters Beta01, Beta02, Beta03, and Beta04; function module ESO4_L. We added the ESO4_L. m program inside Edit.

In the ESO4_L subsystem wrapping process, Transparency in the Icon & Ports property is set to Transparent, and the Drawing commands section is disp ("ESO4_L"). Parameters property in the Parameters property, prompt and variable are set to Beta01, Beta02, Beta03, and Beta04, and their types are edited; the mask type in the documentation property is set to ESO4_L.The modular composition of the expansion state observer subsystem is shown in Figure 14, and the completed ESO4_L subsystem module of the package is shown in Figure 15.

The error feedback control rate subsystem is created, where the specific settings of the tracking differentiator subsystem module are function name CL3_L; function parameters are

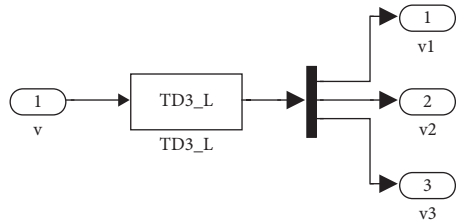


Figure 12: Modular composition of the tracking differentiator subsystem.

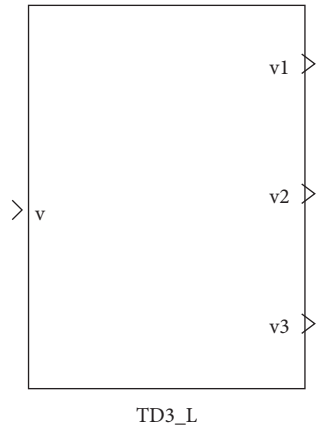


Figure 13: The TD3_L subsystem module after packaging.

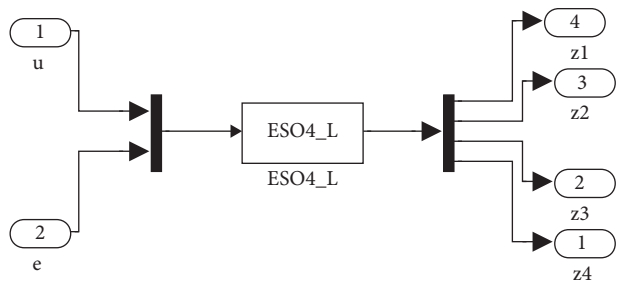


Figure 14: Modular composition of the ESO subsystem.

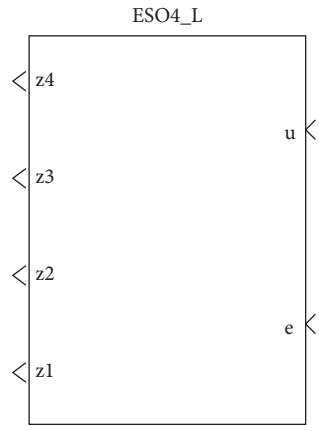


Figure 15: Packaged ESO4_L subsystem module.

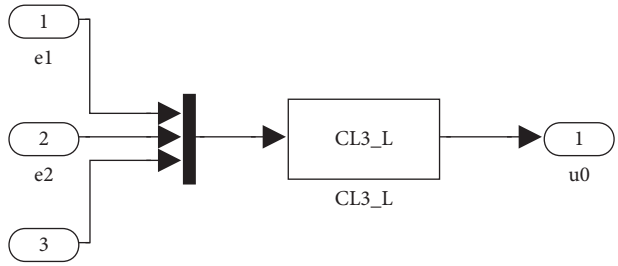


Figure 16: Modular composition of the CL subsystem.

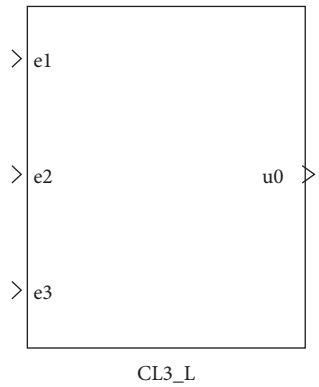


Figure 17: Packaged CL3_L subsystem module.

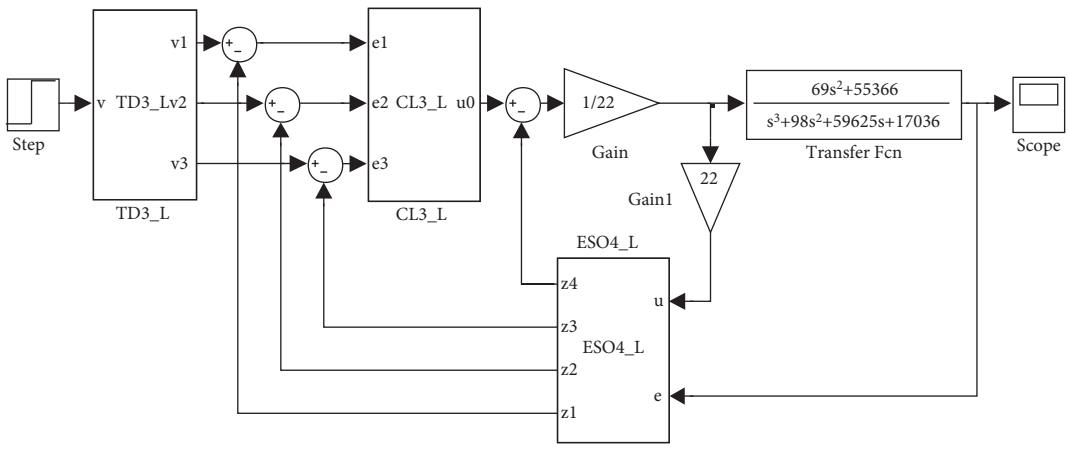


Figure 18: Simulation model of control system self-immunity control.

Beta11, Beta12, and Beta13; function module is CL3_L; and the CL3_L. m program is added inside the edit.

During the packaging of the CL3_L subsystem, Transparency in the Icon & Ports property is set to Transparent, and the Drawing commands section is disp ("CL3_L"); Prompt in the Parameters property and the modular composition of the error feedback control rate subsystem is shown in Figure 16, and the completed CL3_L subsystem module is shown in Figure 17.

*4.4.3. Simulation of Self-Anti-Disturbance Control of the Test Bench Electro-Hydraulic Servo Control System.* Combined with the SIMULINK module, we establish the control system self-anti-disturbance control simulation model, as shown in Figure 18.

The parameter $r$ in the tracking differentiator has the greatest impact on its performance. r too large or too small will change the time of arranging the transition process and the amount of overshoot of the system, and the tracking effect of the system will become poor. The specifics of the change in the performance of the control system with the parameter $r$ are shown in Figures 19 and 20, respectively.

The expansion state observer parameters $\beta_{01}$, $\beta_{02}$, $\beta_{03}$, and $\beta_{04}$ have an impact on its dynamic characteristics. When $\beta_{01}$ increases, the system does not have much effect; when $\beta_{01}$

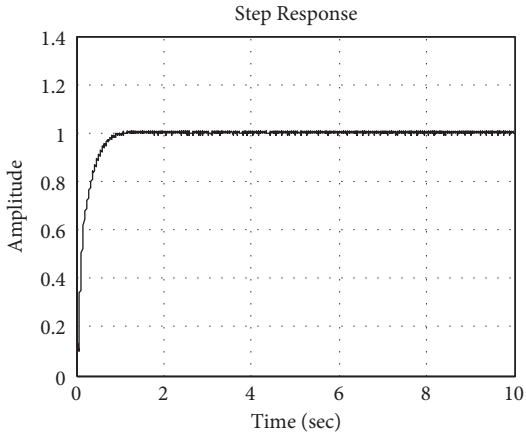


Figure 19: Response curve at 2 times r.

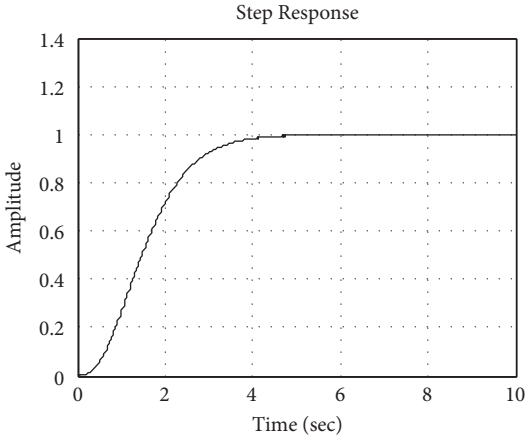


Figure 20: Response curve at 0.1 times r.

decreases, the system will have divergent oscillations. Usually, the value of $\beta_{01}$ is of the same order of magnitude as the reciprocal of the sampling time $h$. The specifics of how the performance of the control system changes with parameter $\beta_{01}$ are shown in Figures 21 and 22, respectively.

When $\beta_{02}$ becomes large, the system emits a noise signal, resulting in reduced system control performance; when $\beta_{02}$ becomes small, the system will increase the number of oscillations, and the amplitude will increase. The details of the change in the performance of the control system with parameter $\beta_{02}$ are shown in Figures 23 and 24, respectively.

When $\beta_{03}$ becomes large, it increases the number of oscillations and the amplitude becomes larger. As $\beta_{03}$ becomes smaller, the system tracking time becomes longer and the oscillation amplitude gradually becomes smaller. The details of the change in the performance of the control system with parameter $\beta_{03}$ are shown in Figures 25 and 26, respectively.

When $\beta_{04}$ becomes large, the system oscillation amplitude becomes larger and the tracking speed slows down; when $\beta_{04}$ decreases, the tracking speed of the system slows

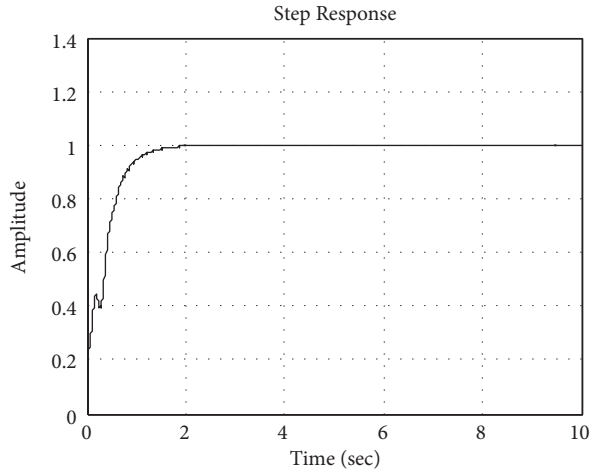


Figure 21: Response curve at 10 times $\beta_{01}$.

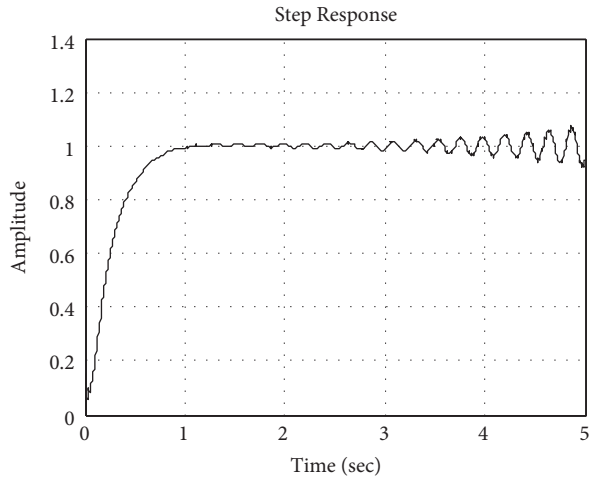


Figure 22: Response curve at 0.1 times $\beta_{01}$.

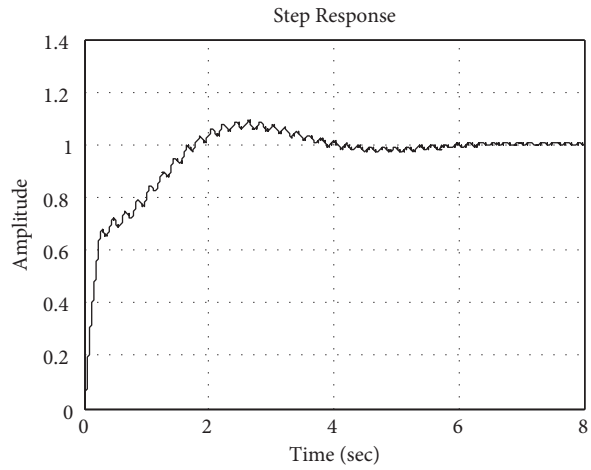


Figure 23: Response curve at 10 times $\beta_{02}$.

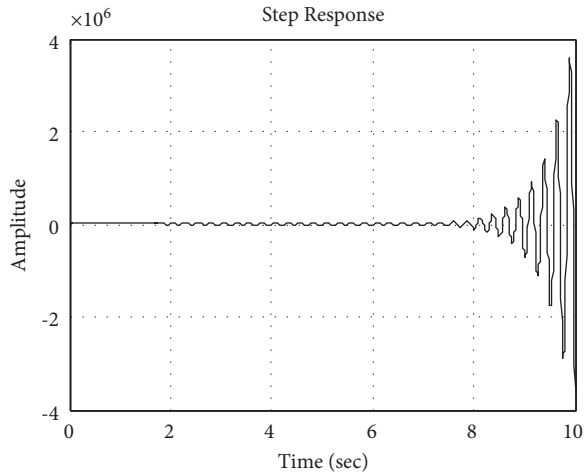


Figure 24: Response curve at 0.1 times $\beta_{02}$.

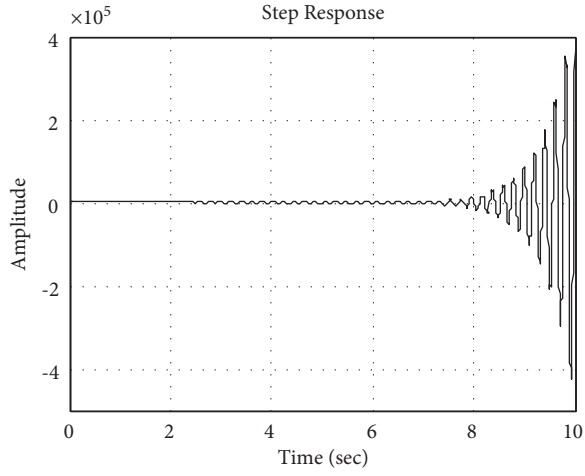


Figure 25: Response curve at 10 times $\beta_{03}$.

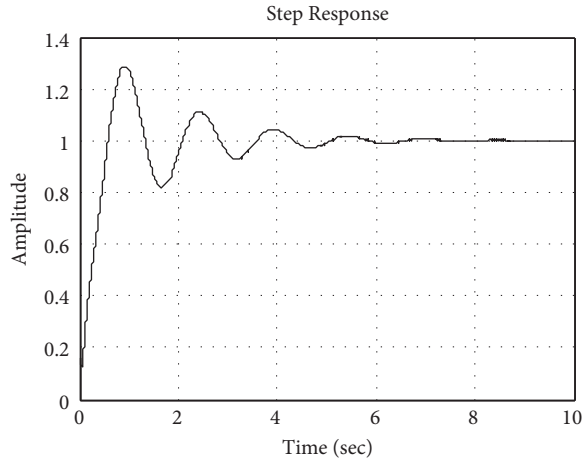


Figure 26: Response curve at 0.1 times $\beta_{03}$.

down substantially and can even cause phase lag. The details of the change in the performance of the control system with parameter $\beta_{04}$ are shown in Figures 27 and 28, respectively.

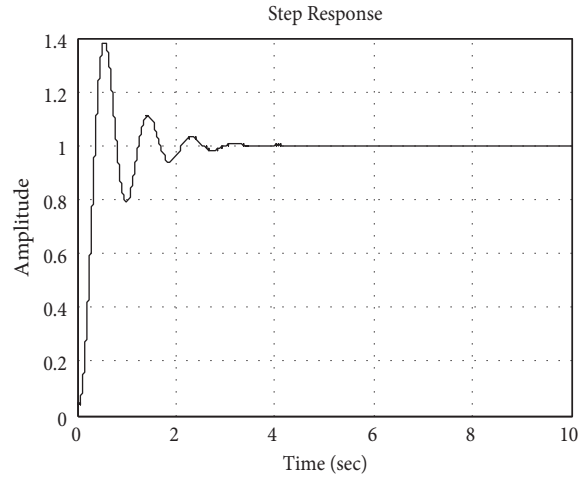


Figure 27: Response curve at 10 times $\beta_{04}$.

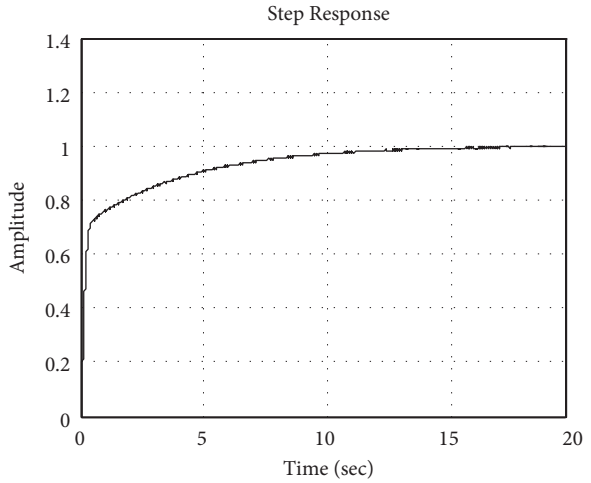


Figure 28: Response curve at 0.1 times $\beta_{04}$.

The parameters $\beta_{11}\beta_{12,}$ and $\beta_{13}$ of the error feedback control rate have an impact on its performance. When $\beta_{11}$ becomes large, the system overshoot increases, making its control quality lower; when $\beta_{11}$ becomes small, the system response is lower than the given signal and the tracking effect is poor. The details of the change in the performance of the control system with parameter $\beta_{11}$ are shown in Figures 29 and 30, respectively.

When $\beta_{12}$ becomes large, the response is lower than the given signal and the tracking effect is poor; When $\beta_{12}$ becomes small, the system oscillates and the amplitude decreases slowly. The details of the change in the performance of the control system with parameter $\beta_{12}$ are shown in Figures 31 and 32, respectively.

When $\beta_{13}$ becomes large, the system responds well; when $\beta_{13}$ is reduced, the system is slightly overshoot. The specifics of how the performance of the control system changes with parameter $\beta_{13}$ are shown in Figures 33 and 34, respectively.

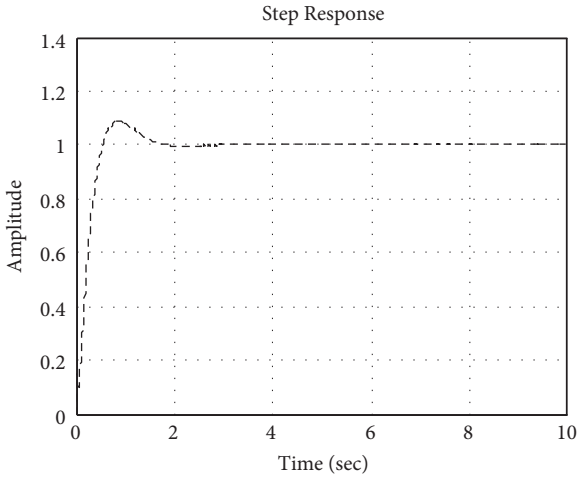


Figure 29: Response curve at 10 times $\beta_{11}$.

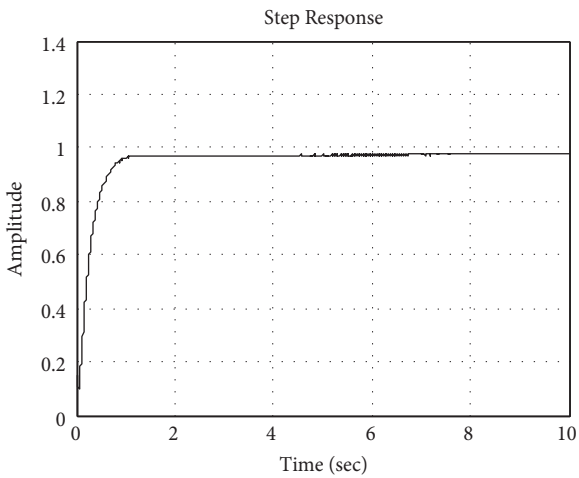


Figure 30: Response curve at 0.1 times $\beta_{11}$.

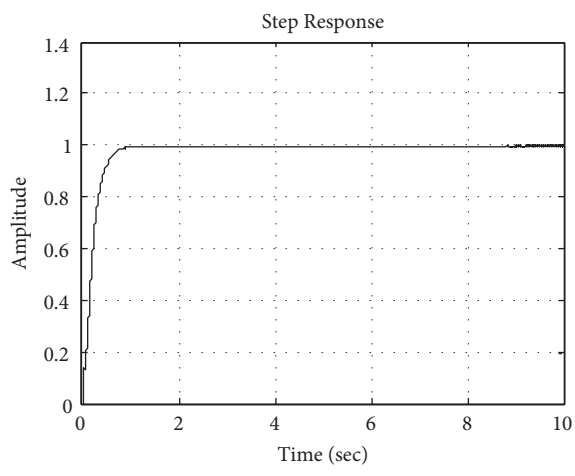


Figure 31: Response curve at 2 times $\beta_{12}$.

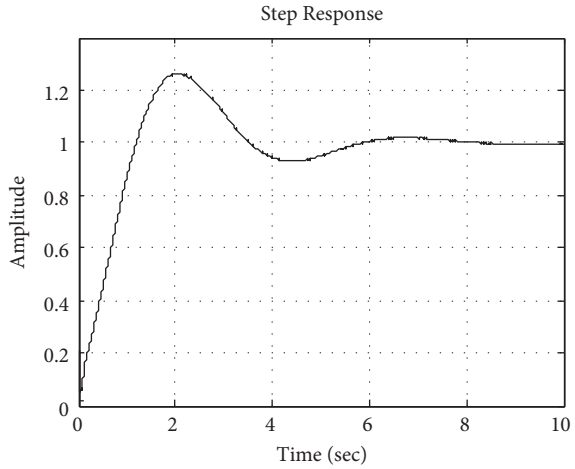


Figure 32: Response curve at 0.1 times $\beta_{12}$.

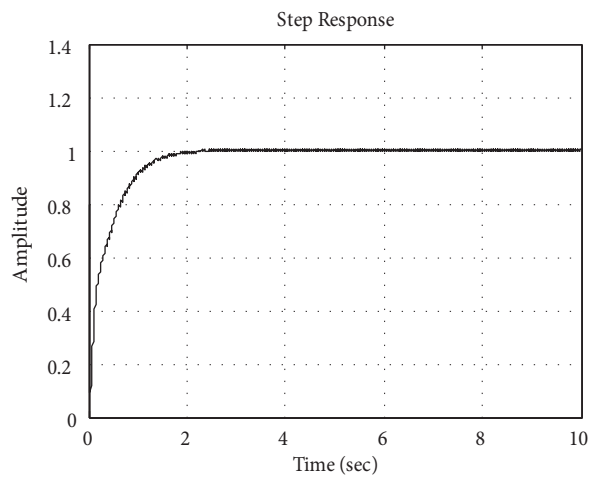


Figure 33: Response curve at 10 times $\beta_{13}$.

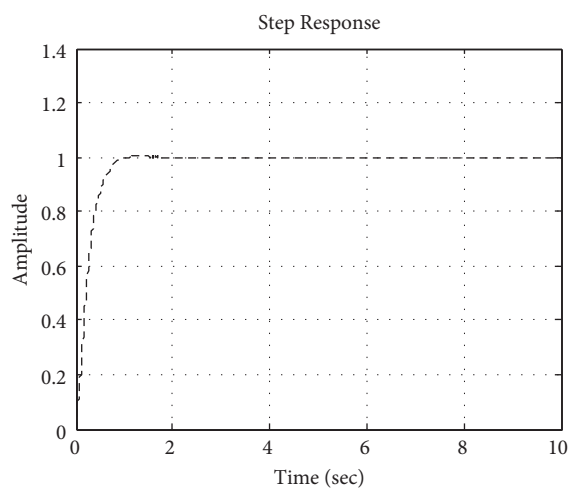


Figure 34: Response curve at 0.05 times $\beta_{13}$.

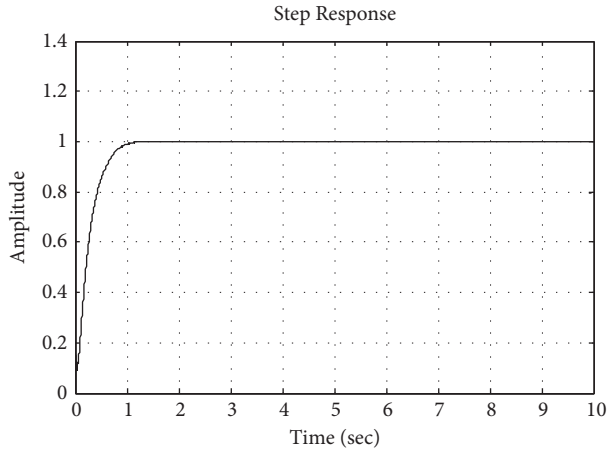


Figure 35: Self-antidisturbance control step response curve of control system.

Setting the parameters of the three modules of the controller separately: TD: $h = 0.1$; ESO: $\beta_{01} = 10$, $\beta_{02} = 680$, $\beta_{03} = 6900$, $\beta_{04} = 22500$; CL: $\beta_{11} = 20$, $\beta_{12} = 70$, $\beta_{13} = 1$, $r = 20$.

By SIMULINK simulation, the control system self-antidisturbance control step response curve is shown in Figure 35.

As can be seen from Figure 35, the servo system self-turbulence control performance is significantly improved. The control system is stable at 1.2 s when a unit step signal is an input and its input and output signals match. As a result, the performance of the servo system is greatly improved after the self-turbulence optimization.

*4.5. Simulation Comparison of Electro-Hydraulic Servo Control System of Test Bench.* To compare the performance advantages and disadvantages of classical PID control, quadratic optimal control, pole configuration, and self-antidisturbance control, SIMULINK is used to build the control system simulation model of the above four optimal control methods, as shown in Figure 36, and the step response curve of the unit step signal under the four control strategies is derived as shown in Figure 37.

From Figure 37, it can be seen that the system has the most stable performance after self-anti-disturbance control. The response speed of PID control is 0.4 seconds slower than that of self-tampering control, and the response is accompanied by a large amount of overshoot; the response time of the pole configuration is 0.2 seconds longer than that of the self-tampering control, and although the overshoot is significantly reduced compared to the PID control, there is still overshoot; neither the secondary type of optimal control nor the self-rejecting control showed overshoot, but the response time of the self-rejecting control was shorter than its response time by 4.4 seconds.

## 5. Test Bench Construction and Experiments

Completed the manufacturing and construction of the test stand, as well as the preparation of the oil film stiffness and thickness adjustment before the experiment, and conducted relevant testing experiments on the test stand.

*5.1. Test Bench Construction.* The basic configuration of the test equipment has a Mitsubishi PLC, touch screen, static floating, and power loading hydraulic control system. The whole hydraulic control system is controlled by a programmable programmer and oil film thickness testing test bench as shown in Figure 38.

*5.2. Testing Test.* First, the oil film stiffness and thickness were adjusted, and then the loading cylinder was controlled by PLC to complete the loading experiment. The detected experimental values are shown in Table 2.

Based on the inspection test datasheet, the following analysis was performed:

(1) The force following case is shown in Figure 39 for the input force as the reference, and the force following effect graph is shown in Figure 39 for the comparison of input force and output force at point a. As can be seen from Figure 39, the deviation of the output force from the input force at point a is between (−2~2) kg, and the force follows well.

(2) Oil film thickness detection accuracy, that is, through the display to observe the oil film thickness at point a, while using a micrometer to measure the oil film thickness at this time. With the micrometer measurement value as the reference, the oil film thickness detection accuracy follows the effect graph as shown in Figure 40. As can be seen from Figure 40, by comparing the detected oil film thickness in both cases, it can be seen that the accuracy of oil film thickness detection is higher.

(3) Analyze the relationship between the loading force and the oil film thickness. For the same action point, it can be seen from the point of Figure 40, with the loading force gradually increasing, the oil film thickness gradually becomes smaller, but the trend of

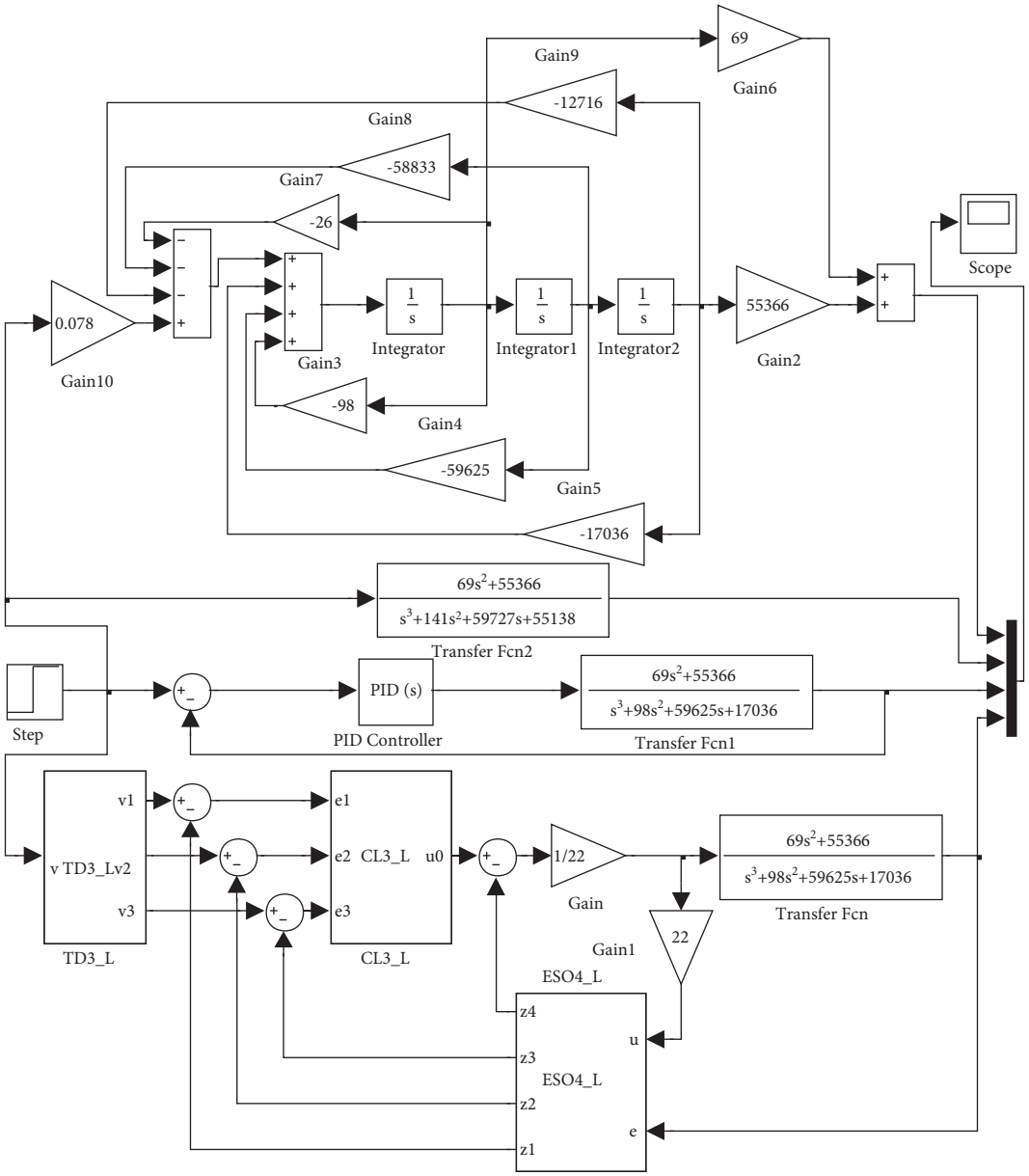


Figure 36: Simulation model of control system based on four control strategies.

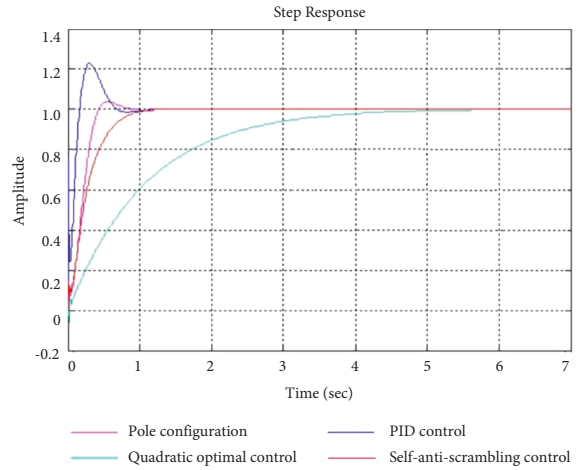


Figure 37: Response curve of control system based on four control strategies.

Figure 38: General assembly of the test bench.

Table 2: Testing experimental values.

| *a* Input force (kg) | a Output force (kg) | a Micrometer oil film thickness ($\mu$m) | a Display oil film thickness ($\mu$m) | a Self-antidisturbance control of oil film thickness ($\mu$m) | b Display oil film thickness ($\mu$m) | c Display oil film thickness ($\mu$m) | d Display oil film thickness ($\mu$m) | e Play oil film thickness ($\mu$m) |
|---|---|---|---|---|---|---|---|---|
| 400 | 402 | 52 | 53 | 46 | 53 | 54 | 52 | 53 |
| 500 | 499 | 45 | 46 | 42 | 45 | 47 | 46 | 47 |
| 600 | 600 | 40 | 40 | 39 | 41 | 39 | 40 | 41 |
| 700 | 702 | 36 | 35 | 36 | 34 | 36 | 36 | 35 |
| 800 | 798 | 31 | 31 | 34 | 31 | 33 | 32 | 31 |
| 900 | 901 | 27 | 28 | 32 | 27 | 28 | 28 | 29 |
| 1000 | 999 | 26 | 26 | 31 | 26 | 25 | 24 | 27 |

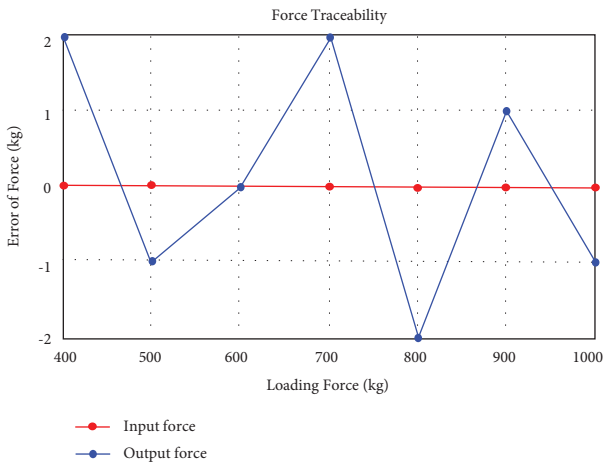


Figure 39: Force following effect.

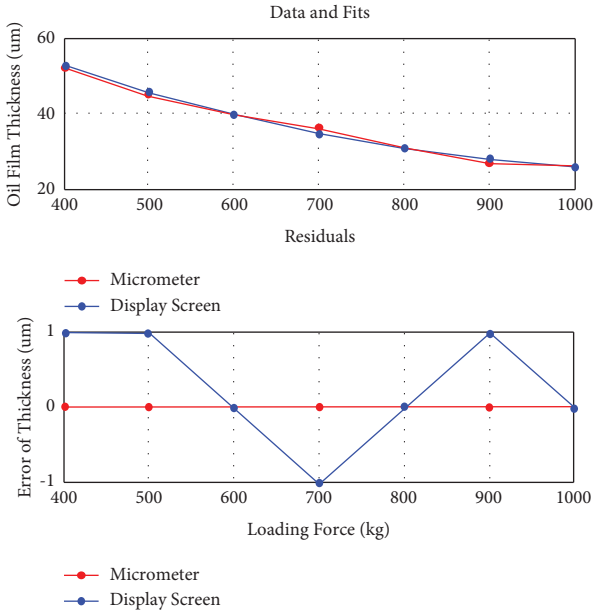


Figure 40: Detection accuracy following effect graph.

becoming smaller is slowing down. For the analysis of different action points, the oil film thickness of five points in Table 2 shows that the oil film thickness does not differ much when the same loading force is loaded at different points.

(4) The change curve of oil film thickness before and after the self-turbulence control is shown in Figure 41. As can be seen from Figure 41, after adding the self-turbulence controller, the change in the oil film thickness of the rail is much slower when it is under load, making the oil film thickness more stable.

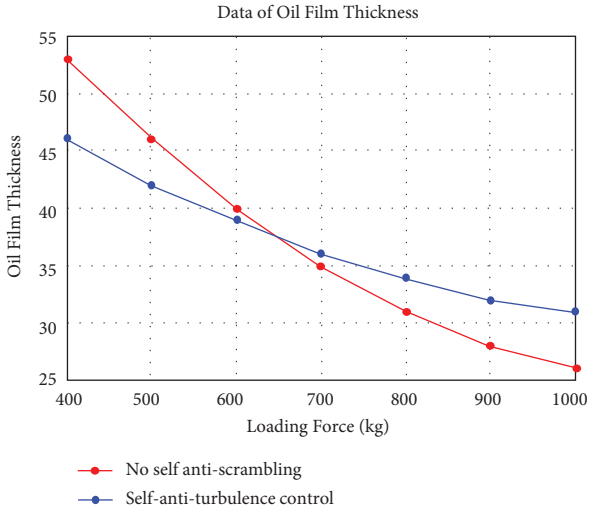


Figure 41: Oil film thickness variation curve.

## 6. Conclusion

The main research elements of this paper are as follows:

(1) This paper designed the overall plan of the test bench, which includes the test bench mechanical structure, electro-hydraulic force servo control system, oil film thickness detection system, and electro-hydraulic force servo control system original parts selection. This study established a three-dimensional model of the test bench by NX and obtained the transfer function of the system through the hydraulic control valve flow equation, the cylinder flow continuity equation, the force balance equation between the cylinder and the load, and combined it with the control system deviation voltage signal equation and the feedback link pressure sensor equation, and finally simulated and analyzed the system.

(2) Using the fast overshoot of PID control, this study introduced a self-anti-disturbance control algorithm and designed the specific structure of the self-anti-disturbance controller. Also, the creation and packaging of the subsystem were completed using zero-pole phase elimination, algorithms for each module, corresponding programming, and customization of the module library. Then the electro-hydraulic servo system of the test bench was optimized by using quadratic optimal control, pole configuration, PID control, and self-turbulence control, respectively. The SIMULINK module was also used to simulate the test bench control system, and then the response curves of the four control strategies were obtained. The results showed that the response speed of the self-tampering control was 0.4 sec, 0.2 sec, and 4.4 sec faster than that of the PID control, pole configuration, and quadratic optimal control, respectively, and the overshoot was significantly reduced.

(3) According to the overall scheme design of the test bench and the design requirements of the relevant technical scheme parameters, this study completed the assembly of the test equipment. The experimental results showed that after adding the self-anti-disturbance control algorithm, the anti-disturbance ability of the electro-hydraulic servo control system of the test bench was improved, the followability of the loading force and the thickness detection accuracy of the test bench were the best, and the stability of the rail oil film thickness was significantly improved.

## Data Availability

The data used to support the findings of this study are included within the article.

## Conflicts of Interest

The authors declare that they have no conflicts of interest.

## Acknowledgments

This work was supported by the major projects of the "The University Synergy Innovation Program of Anhui Province (GXXT-2019-004)" and "Teaching Research Project of Anhui Education Department (2019jyxm0229)."

## References

[1] D. Wang, "Research on hydrostatic guideway and its application in the design of machine tool guideway," *Hydraulic Pneumatics and Seals*, no. 5, pp. 26–28, 2003.

[2] J. Gong, Y. Zhao, and Q. Liu, "Static characteristics and flow field simulation analysis of hydrostatic guide for ultra-precision positioning table," *Machine Tools and Hydraulics*, vol. 43, no. 7, pp. 46–50, 2015.

[3] W. Wu, J. Gao, J. G. Lu, and X. Li, "On continuous-time constrained stochastic linear–quadratic control," *Automatica*, vol. 114, Article ID 108809, 2020.

[4] R. Dario and T. Iacopo, "Active control of linear vibrating systems for antiresonance assignment with regional pole placement," *Journal of Sound and vibrationvolume*, vol. 494, Article ID 115858, 2021.

[5] B. Yang, W. Li, Z. Jiang, T. G. Shi, G. Y. Wu, and Y. J. Sun, "Disturbance rejection control of Industrial Heavy-load hydraulic force servo system," *Acta Automatica Sinica*, vol. 35, no. 7, pp. 926–932, 2009.

[6] L. Ji-min, L. Yeong-Cheng, and L.-J. Zhu, "Optimization of PID parameters with an improved simplex PSO," *Journal of Inequalities and Applications*, vol. 2015, no. 1, pp. 1–5, 2015.

[7] Y. Li and X. Cao, "Research on electro-hydraulic servo control system," *Industrial Control Computer*, vol. 29, no. 7, pp. 38–40, 2016.

[8] Q. Gao, L. Qian, and L. Huang, "Application of active disturbances rejection contror in electro-hydraulic position servo system of pump-controlled cylinder," *Electrical Automation*, vol. 36, no. 8, pp. 121-122, 2008.

[9] F. J. Goforth, Q. Zheng, and Z. Gao, "A novel practical control approach for rate independent hysteretic systems," *ISA Transactions*, vol. 51, no. 3, pp. 477–484, 2012.

[10] B. Wang, P. Jiang, and Y. Lin, "Creation of a custom module library for self-turbulent control techniques in SIMULINK," *Journal of System Simulation*, vol. 22, no. 3, pp. 610–615, 2010.
[11] Z. Wang, *Research on Self-Anti-Disturbance Control Theory and its Application in Cold Rolling*, University of Science and Technology Beijing, Beijing, China, 2015.
[12] E. Qi, Z. Fang, T. Sun, J. Chen, C. Liu, and J. Wang, "A method for predicting hydrostatic guide error averaging effects based on three-dimensional profile error," *Tribology International*, vol. 2016, p. 95, 2016.
[13] H. G. Kim, J. W. Lee, Y. H. Choi, J. W. Park, and J. H. Suh, "Simulations and experiments on the force control of hydraulic servo system for hydraulic Robots," *Applied Mechanics and Materials*, vol. 826, pp. 128–133, 2016.
[14] M. Han, Y. Song, W. Zhao, Y. Cheng, and J. Xiang, "Simulation and optimization of synchronization control system for CFETR water hydraulic manipulator based on AMEsim," *Journal of Fusion Energy*, vol. 34, no. 3, pp. 566–570, 2015.
[15] M. Antonelli, A. Baccioli, M. Francesconi, P. Psaroudakis, and L. Martorano, "Small Scale ORC plant modeling with the AMESim simulation tool: analysis of working fluid and thermodynamic cycle parameters Influence," *Energy Procedia*, vol. 81, pp. 440–449, 2015.
[16] L. Prasad, B. Tyagi, and H. O. Gupta, "Optimal control of nonlinear Inverted Pendulum system using PID controller and LQR: performance analysis without and with disturbance input," *International Journal of Automation and Computing*, vol. 11, no. 6, pp. 661–670, 2014.
[17] P. D. Mandić, T. B. Šekara, M. P. Lazarević, and M. Boskovic, "Dominant pole placement with fractional order PID controllers: D-decomposition approach," *ISA Transactions*, vol. 67, pp. 76–86, 2017.
[18] G. Fan, *Design and Research of Intelligent PID Control System*, Zhejiang University of Technology, Hangzhou, China, 2005.
[19] M. Krstic, "On the applicability of PID control to nonlinear second-order systems," *National Science Review*, vol. 4, no. 5, p. 668, 2017.
[20] J. Li, Y. Xia, X. Qi, Z. Gao, K. Chang, and F. Pu, "Absolute stability analysis of non-linear active disturbance rejection control for single-input–single-output systems via the circle criterion method," *IET Control Theory & Applications*, vol. 9, no. 15, pp. 2320–2329, 2015.
[21] J. Han, *Self-Disturbance Control Techniques-Control Techniques for Estimating Compensation Uncertainties*, Defense Industry Press, Arlington, Virginia, 2016.
[22] C. Fu and W. Tan, "Control of unstable processes with time delays via ADRC," *ISA Transactions*, vol. 71, no. 2, pp. 530–541, 2017.
[23] B. Gao, J. Shao, and X. Yang, "A compound control strategy combining velocity compensation with ADRC of electro-hydraulic position servo control system," *ISA Transactions*, vol. 53, no. 6, pp. 1910–1918, 2014.
[24] J. Li, X. Qi, and S. Qi, "A quadrotor attitude decoupling control method based on self-anti-disturbance technique[J]," *Electronics Optics and Control*, vol. 20, no. 3, pp. 44–48, 2013.